ACSNANO

www.acsnano.org

ARTICLE

High-Speed Atomic Force Microscopy Reveals Loss of Nuclear Pore Resilience as a Dying Code in Colorectal Cancer Cells

Mahmoud Shaaban Mohamed,[†,‡,§] Akiko Kobayashi,[†,§] Azuma Taoka,[‡,§] Takahiro Watanabe-Nakayama,[‡] Yosuke Kikuchi,[§] Masaharu Hazawa,[†,§] Toshinari Minamoto,[∥] Yoshihiro Fukumori,[§] Noriyuki Kodera,[‡] Takayuki Uchihashi,[‡] Toshio Ando,[‡] and Richard W. Wong*[,†,‡,§]

[†]Cell-Bionomics Research Unit, Innovative Integrated Bio-Research Core, Institute for Frontier Science Initiative, [‡]Bio-AFM Frontier Research Center, [§]Division of Natural System, School of Natural Science and Technology, and [∥]Division of Translational and Clinical Oncology, Cancer Research Institute, Kanazawa University, Kakuma-machi, Kanazawa 920-1192, Japan

Supporting Information

ABSTRACT: **Nuclear pore complexes (NPCs) are the sole turnstile implanted in the nuclear envelope (NE), acting as a central nanoregulator of transport between the cytosol and the nucleus. NPCs consist of ∼30 proteins, termed nucleoporins. About one-third of nucleoporins harbor natively unstructured, intrinsically disordered phenylalanine-glycine strings (FG-Nups), which engage in transport selectivity. Because the barriers insert deeply in the NPC, they are nearly inaccessible. Several *in vitro* barrier models have been proposed; however, the dynamic FG-Nups protein molecules themselves are imperceptible *in vivo*. We show here that high-speed atomic force microscopy (HS-AFM) can be used to directly visualize nanotopographical changes of the nuclear pore inner channel in colorectal cancer (CRC) cells. Furthermore, using MLN8237/alisertib, an apoptotic and autophagic inducer currently being tested in relapsed cancer clinical trials, we unveiled the functional loss of nucleoporins, particularly the deformation of the FG-Nups barrier, in dying cancer cells. We propose that the loss of this nanoscopic resilience is an irreversible dying code in cells. These findings not only illuminate the potential application of HS-AFM as an intracellular nanoendoscopy but also might aid in the design of future nuclear targeted nanodrug delivery tailored to the individual patient.**

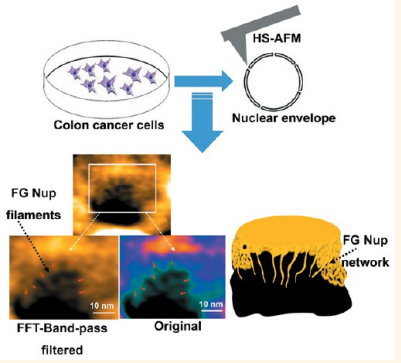

KEYWORDS: *high-speed atomic force microscopy, live cell imaging, nanopore, nuclear pore complex, colon cancer*

Metastasis is the primary cause of morbidity and death in most cancers, and it is facilitated by numerous growth factors and cytokines, which operate through various signaling pathways.[1,2] All metastatic signaling pathways must enter into the nucleus through a single nanodoorkeeper, the nuclear pore complex (NPC).[1,3] NPCs act as the sole turnstiles between the nucleus and the cytoplasm.[4,5] They are biological "nanomachines" assembled inside the cell that are composed of varying copy numbers of around 30 different proteins called nucleoporins.[6,7] Transport through NPCs is very selective and vigorous with respect to ultrastructural perturbations and molecular noise. Small molecules can pass freely through NPCs;[8] in contrast, larger molecules (>40 kDa) can pass through the pore smoothly only if they are bound to specific transporter proteins that interact with FG (phenylalanine-glycine)-nucleoporins (FG-Nups), which form a soft and flexible lining composed of approximately 200 intrinsically disordered polypeptide chains inside the turnstile.[9−12] Several FG-Nup trafficking models have been proposed, such as forest,[13] virtual gating,[9] polymer brush,[10,14] and selective phase/hydrogel[11] models. Unfortunately, there has been a lack of techniques that can visualize and investigate FG-Nup behavior inside the NPCs of cancer cells. Additionally, the concomitant assessment of nanoscopic structures and dynamics has been technically unfeasible, a situation prevailing throughout cell biology research.[15] This lack of experimental devices and scarcity of sufficient measurement precision to investigate the FG-Nups *in vivo* on the pertinent length (nanometer) and time (millisecond) scales[12,16] has prevented a full understanding of NPC transport in cancer cells.

Conventional atomic force microscopy (AFM) approaches, which typically use *Xenopus* egg nuclear pores, have revealed static snapshots and stiffness measurements at relatively slow speeds,[17,18] and these have lacked the necessary spatial

Received: February 9, 2017
Accepted: May 22, 2017
Published: May 22, 2017

DOI: 10.1021/acsnano.7b00906
ACS Nano 2017, 11, 5567−5578

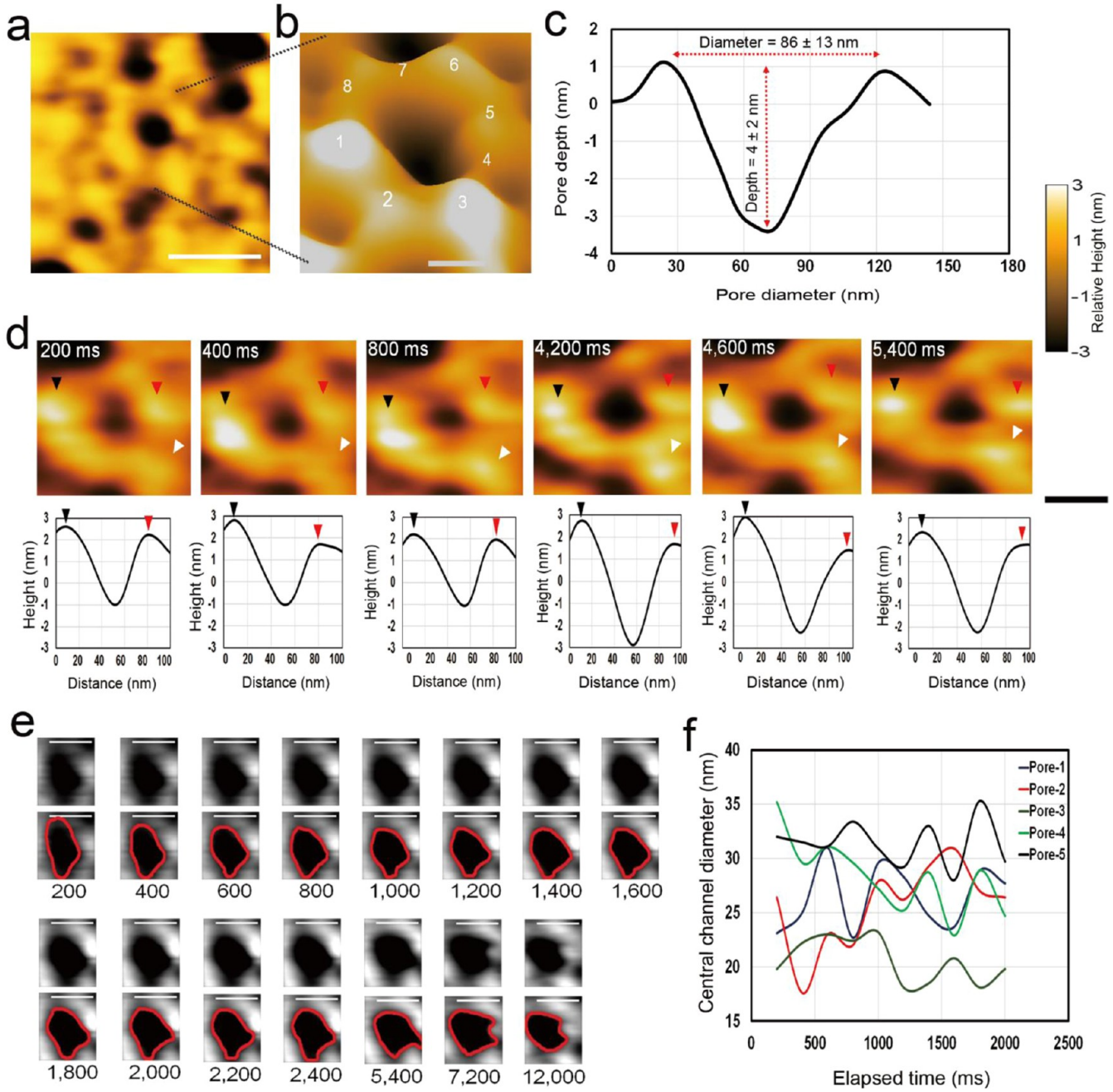

Figure 1. HS-AFM observation of native human NPCs. (a) HS-AFM frame showing the NE cytoplasmic face with many NPCs averaged from 74 frames (Z-scale = 6 nm, speed = 5 frames/s) with 200 × 200 pixels; scale bar, 100 nm. (b) 3D view of a single representative NPC (Z-scale = 6 nm, speed = 5 frames/s) with 200 × 200 pixels; scale bar, 50 nm. (c) Cross-section of human colon cancer NPCs with an overall diameter of 86 ± 13 nm when measured from maxima of opposing filaments, where the central channel diameter is 33 ± 2 nm and pore maxima depth is 4 ± 2 nm (n = 110). (d) Dynamic rapid changes of NPC cytoplasmic filaments in the shown HS-AFM frames at different time points at the millisecond scale (black, red, and white arrows) (Z-scale = 8 nm, speed = 5 frames/s) with 200 × 200 pixels; scale bar, 50 nm. (e) Successive frames of a native NPC central channel showing the dynamic changes of the channel shape and diameter over time. The numbers below each frame correspond to the elapsed time (Z-scale = 6 nm, speed = 5 frames/s) with 200 × 200 pixels; scale bar, 50 nm. (f) Central channel diameter changes over time plotted against the elapsed time (ms).

resolution to assess the central channel of FG-Nups. Although *Xenopus* oocytes are an ideal model in which to study nucleocytoplasmic transport owing to their large size (1000 μm) when compared with mammalian nuclei (10−20 μm), which facilitates the isolation of nuclear envelopes (NEs),[19] there are composition and functional differences in the NPCs between species.[20] For example, cell division processes,[18] NE rupture and repair during cancer cell migration,[5] the role of oncogenes or tumor suppressors in viral trafficking, and chromatin modifications in mammalian cell NPCs are all substantially dissimilar to those in the NPCs of *Xenopus* eggs. Therefore, there is an urgent need to investigate the spatiotemporal dynamics of mammalian NPCs.[20] The development of high-speed AFM (HS-AFM) has led to instruments that surmount previous limitations, with subsecond temporal and subnanometer spatial resolution.[21−24] Inspired by the

DOI: 10.1021/acsnano.7b00906
ACS Nano 2017, 11, 5567−5578

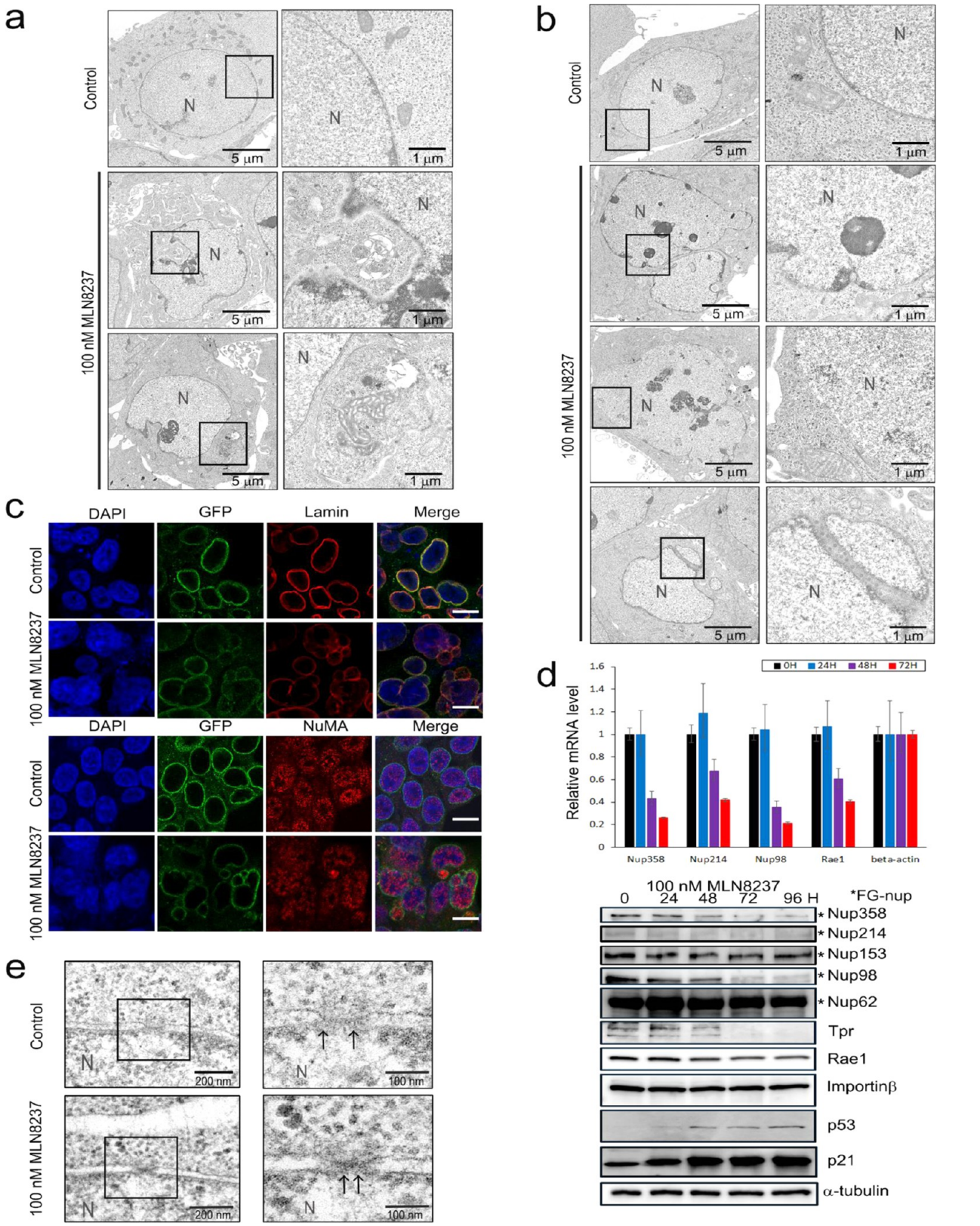

Figure 2. Effects of MLN8237 (alisertib) treatment in HCT116 cells. (a) Electron microscopy images of control or MLN8237-treated HCT116 mitotic cells. Scale bars, 250 nm. N denotes the nucleus. (b) Micrographs of control or MLN8237-treated HCT116 mitotic cells. Scale bars, 250 nm. (c) Confocal images of MLN8237-treated GFP-Nup358 stable HCT116 cells, stained with GFP (green) and Lamin A/C (red, upper) or NuMA (red, lower) at the indicated concentrations. Goat anti-mouse Alexa Fluor-488 or rabbit rhodamine was used as secondary antibodies. DNA was counterstained using 4′,6-diamidino-2-phenylindole (DAPI). Scale bar, 10 μm. (d) HCT116 cells were treated with MLN8237 for 24, 48, 72, or 96 h at 100 nM and then analyzed by qPCR (mRNA level, upper panels) or immunoblot (protein level, lower panels) with the indicated antibodies. (e) Micrographs of control or MLN-treated HCT116 cells. Insets are magnifications of the nuclear envelope (NE) and nuclear pore regions in the observed cells. N denotes the nucleus.

DOI: 10.1021/acsnano.7b00906
ACS Nano 2017, 11, 5567−5578

recent step forward of studies using HS-AFM to record the nuclear pore of *Xenopus* eggs,[25] we decided to investigate the native nanoscopic dynamics of the human nuclear pore turnstile in cancer cells. Here, we overcame several technical barriers to optimize the NE purification procedures and refine the fluorescent and HS-AFM movie recording techniques. First, we added sensitive fluorescence microscopy[26] into our HS-AFM system to visualize individual NPC proteins (upper filament nucleoporin Nup358/RanBP2 was fused with a GFP tag; Supplementary Figure 1).[24,27,28] Second, for cantilever improvements, we constructed a homegrown electron beam deposition (EBD) tip under a scanning electron microscope (SEM) that was approximately 2 μm long and had a tip radius of approximately 8 nm during imaging (Supplementary Figure 2).[28] Third, we isolated the NE and NPCs from human colorectal cancer (CRC) HCT116 cells[29] and further confirmed the NE purification by negative stain electron microscopy (EM) and confocal microscopy (Supplementary Figure 3). To further support our HS-AFM studies, we also combined high-resolution live cell imaging and EM to explore the native nanoscopic spatiotemporal dynamics in NPC ultrastructural organizations in the CRC cells.

RESULTS AND DISCUSSION

Figure 1a shows a single frame from an HS-AFM movie of the cytosol-facing outer nuclear membrane with few NPCs (Movie 1a). A single NPC with its centrally located channel is displayed in Figure 1b, which was averaged over 100 frames that were recorded at 5 frames/s (Movie 1b). We often found individual NPCs with approximately eight globular ring-like features facing the cytosol (Figure 1a,b). Consistent with recent reports in *Xenopus*,[25] we also observed considerable pore-to-pore variability, and depending on different phases in the cell cycle, we sometimes (but not always) found a nuclear plug-like structure in the central lumen of the NPC (Supplementary Figure 4a,b). There are controversial opinions on the functions of those central granules as components of the NPC or "central plugs" or "transporter" (CP/T) or "cargoes in transit"[30,31] or disease-related peptides directly obstructing the central channel of the NPC.[32,33] Furthermore, since their presence would be hazy in the central channel (FG repeats) observation, in this paper, we focus on the pores that lack of those plugs. We also prefixed NE with 5% paraformaldehyde and found that the overall structure of the basket of NPC has a diameter of ~120 nm, whereas the distal ring was approximately ~50 nm in diameter (Supplementary Figure 4; Movie 2). We analyzed approximately 110 NPCs from HCT116 cells and calculated the mean values of cytoplasmic filaments. They were 4 ± 2 nm in depth, and the outer diameter of the cytosolic rings was 86 ± 13 nm, which is quite consistent with previous snapshots of NPCs from other mammalian cells in conventional AFM studies;[34−36] however, HCT116 cells' NPCs were moderately different in depth compared with *Xenopus* egg NPCs[25] (Figure 1c). Figure 1d shows selected successive snapshots of the same region in an outer nuclear ring, highlighting the sequential changes in the motion of cytoplasmic surfaces recorded at 200 ms/frame in another separate recording. We plotted their $x-y$ directional displacement and height and found that they adopted extending or retracting dynamic spatial conformations (Figure 1d and Movie 1c). Indeed, the inner nuclear central channel also showed sequential changes in motion, probably caused by FG-Nups, under the elapsed time of 200 ms/frame (Figure 1e; Movie 1d). We further investigated these sequential playbacks and found a remarkable independent dynamic behavior in five representative inner channels (Figure 1f). Together, these data indicate that HS-AFM can be used to record the native spatiotemporal dynamics of NPCs in cancer cells.

The nanoscopic structural and molecular sequential events of NEs and NPCs in autophagic and apoptotic cell death are largely unknown. To gain insights into the cell dying process, we used MLN8237 (Alisertib), which is a selective Aurora kinase A inhibitor that is currently undergoing phase I−III clinical trials[37] for relapsed cancer treatments (www.clinicaltrials.gov)[38] and has been demonstrated to prevent proliferation and induce autophagy, apoptosis, and senescence.[39] We analyzed the molecular and mechanistic outcomes of MLN8237-treated NPCs. MLN8237 treatment induced cell cycle arrest and promoted centrosome abnormality and mitotic cell death (Movie 3a,b) in HCT116 cells (Supplementary Figure 5). To observe the changes in nuclear morphology, we performed EM, confocal microscopy, and live cell imaging. We frequently found nuclear deformation with membranous vacuoles after 48 h of MLN8237 treatment in HCT116 cells (Figure 2a). Using confocal and total internal reflection microscopy and live cell imaging of GFP-Nups or NE proteins (GFP-Lamin B1, GFP-Nup358, or GFP-Nup98 and GFP-Tpr), we revealed that MLN8237 treatment also induced multinuclei formation (Movie 4a), nuclear fusion (Movie 4b,c), nuclear budding (Movie 4d), NE rupture (Movie 4e), and nuclear fragmentation (Figure 2b,c). Further, MLN8237 treatment inhibited NPC mRNA and protein expression (Figure 2d; Movie 5a−d) before cell death. Interestingly, the expression of FG-Nup98 was reduced, but that of FG-Nup62 was not changed in the MLN8237-treated NEs (Figure 2d). These data are consistent with the ideas that FG-Nup62 complexes seem to be replaceable for basic NPC function and that Nup98 is necessary for both active and passive transport.[11,19] Notably, using EM, we determined that there were 7.7 ± 0.82 nuclear pores/μm^2 in HCT116 cells, which was close to our previously published values in HeLa cells.[40] However, there were only 4.4 ± 0.52 nuclear pores/μm^2 in MLN8237-treated cells (n = 90 pores from 3 sets of micrographs in control and MLN8237-treated respectively; Supplementary Figure 6). We also found that NPC diameters were reduced ~40% after MLN8237 treatment (Figure 2e, n = 32 pores, micrographs in control and MLN8237-treated, respectively).

Mechanistically, MLN8237 treatments induced p53-p21 oncogene-induced senescence[41] (Figure 2d) and activated the autophagy marker LC3 (Supplementary Figure 7a−d). As a result, the FG-Nups (Figure 2d) were reduced and the flexible barriers of the pores were lost, further driving cytoplasmic LC3 and other proteins into the nuclei (Movie 5b−d) and facilitating interaction between nuclear membrane protein Lamin B1[42] and nucleoporins (Supplementary Figure 7). NE blebs, budding, exocytosis, and nucleophagy (Movie 5e) were also induced in dying cells. Further, the endosomal sorting complexes for the transport III (ESCRT III) family were reported to be involved in resealing the NE in cell migration.[5] We found that unlike NE rupture and repair during cancer cell migration, the mRNA expression levels of ERSCRT III were decreased in dying cells (Supplementary Figure 7e), which might explain why the NEs that were ruptured after MLN8237 treatment could not be repaired. Together, these results indicate that MLN8237 is a suitable chemical for studying

DOI: 10.1021/acsnano.7b00906
ACS Nano 2017, 11, 5567−5578

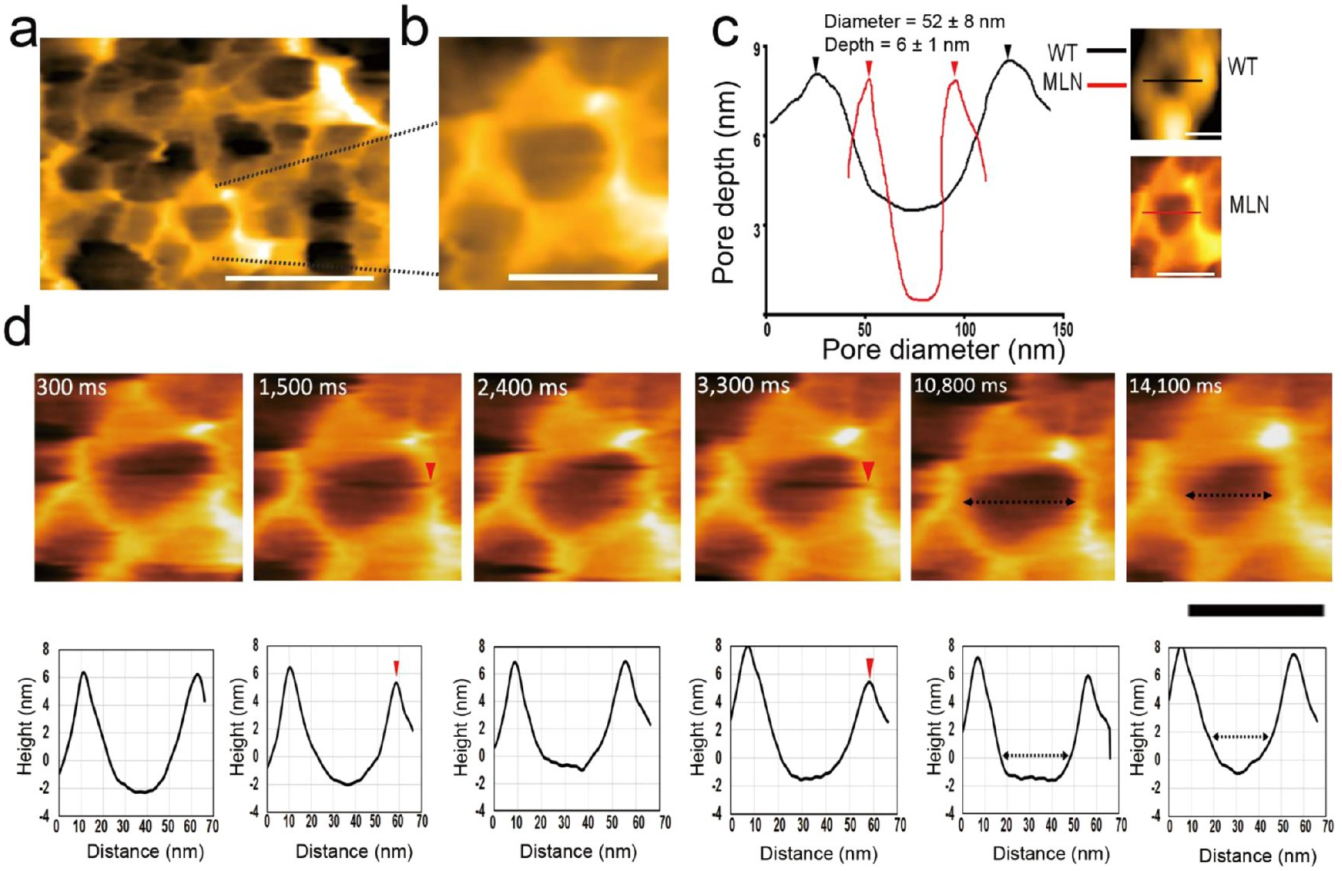

Figure 3. HS-AFM observation of NPC changes in dying HCT116 cells. (a) Morphology and dynamics of native HCT116 NPCs after treatment with MLN8237 (100 nM, 48 h) (Z-scale = 20 nm, speed = 3.3 frames/s) with 200 × 200 pixels; scale bar, 100 nm. (b) Single representative dying NPC (Z-scale = 20 nm, speed = 3.3 frames/s) with 200 × 200 pixels; scale bar, 50 nm. (c) Comparison plot showing differences in diameter and depth between wild-type (WT, n = 110) and MLN8237-treated NPCs (n = 85). The pore diameter of the treated pores is 53 ± 9 nm, their depth is 6.5 ± 1 nm, and their central channel diameter is 28 ± 5 nm. (d) HS-AFM frames captured at different time points at the millisecond scale showing the dynamic changes of dying NPC after treatment with MLN8237. The pore diameter is marked by black dotted arrows. Red arrows indicate changes in the NPC filaments. Z-scale = 20 nm, speed = 3.3 frames/s with 200 × 200 pixels; scale bar, 50 nm.

rapid nuclear dynamics, as it can interfere with nuclear morphology and reduce NE and NPC activities in CRC cells.

On the basis of the above results, we further explored the possibility of using HS-AFM to visualize the ultrastructure of individual NPCs after treating GFP-Nup358 HCT116 cells with 100 nM MLN8237 for 48 h. The HS-AFM results revealed that treatment with MLN8237 highly affects the extrafine structural organization of the NPC nucleoplasmic faces. The NPC rim in MLN8237-treated cells was patterned by distinctive elevated structures, which most likely indicate that the cytoplasmic filaments were softer than those of NPCs in control DMSO-treated cells, perhaps as a result of degradation of the cytoplasmic filaments of the doomed NPC upon inhibitor treatment (Figure 3a,b; Movie 6a,b). Our HS-AFM analysis of NPCs also showed that the upper rim diameter of MLN8237-treated NPCs (n = 85) was narrower (53 ± 9 nm), but the depth was deeper (7 ± 1 nm) than that of control NPCs (n = 110) (Figure 3c; Movie 6a,b). Furthermore, the results observed with HS-AFM are paralleled by our immunoblot and EM data, which showed the degradation and reduction of Nups and a narrowing of the central channel (Figure 2d,e; Movie 6a,b). Dynamic spatial conformations were also found when we plotted their x−y directional displacement and height (Figure 3d; Movie 6b). The selected continuous snapshots of the same region in the outer nuclear ring highlight the sequential changes in the motion of cytoplasmic surfaces at 300 ms/frame in other separate recordings of outer nuclear rings.

To determine FG-Nup behavior, we concentrated on the central turnstile enclosed by the cytoplasmic filaments and raised the scan rate to 6.7 frames/s (150 ms/frame). A postexperiment image registration algorithm was then adopted to align successive frames in the x−y plane and to rectify for drift in the z direction[25] (see Methods). We visualized native and drug-treated FG-Nups by HS-AFM. In particular, the extended and retracted FG-Nups appeared to have a brush-like conformation (Figure 4a−c). We speculate that FG-Nup transport with different physical properties of both entropic ("brush-like") and enthalpic/cohesive hydrophobic ("gel-like") concepts may be reconciled in the near future.[12]

Further implementing basic image filtering revealed a waving and beating motion of FG-Nups that frequently extended into and retracted from the central turnstile (Figure 5a; Movies 7−10). This finding is similar to those observed by HS-AFM in studies of intrinsically disordered proteins[43] and of *Xenopus* NPC FG-Nups.[25] FG-Nups are short, stiff, hair-like, twisted ropes that together have a brush-like manner or form a broken cobweb shape from their tethering point,[10] which suggests the

DOI: 10.1021/acsnano.7b00906
ACS Nano 2017, 11, 5567−5578

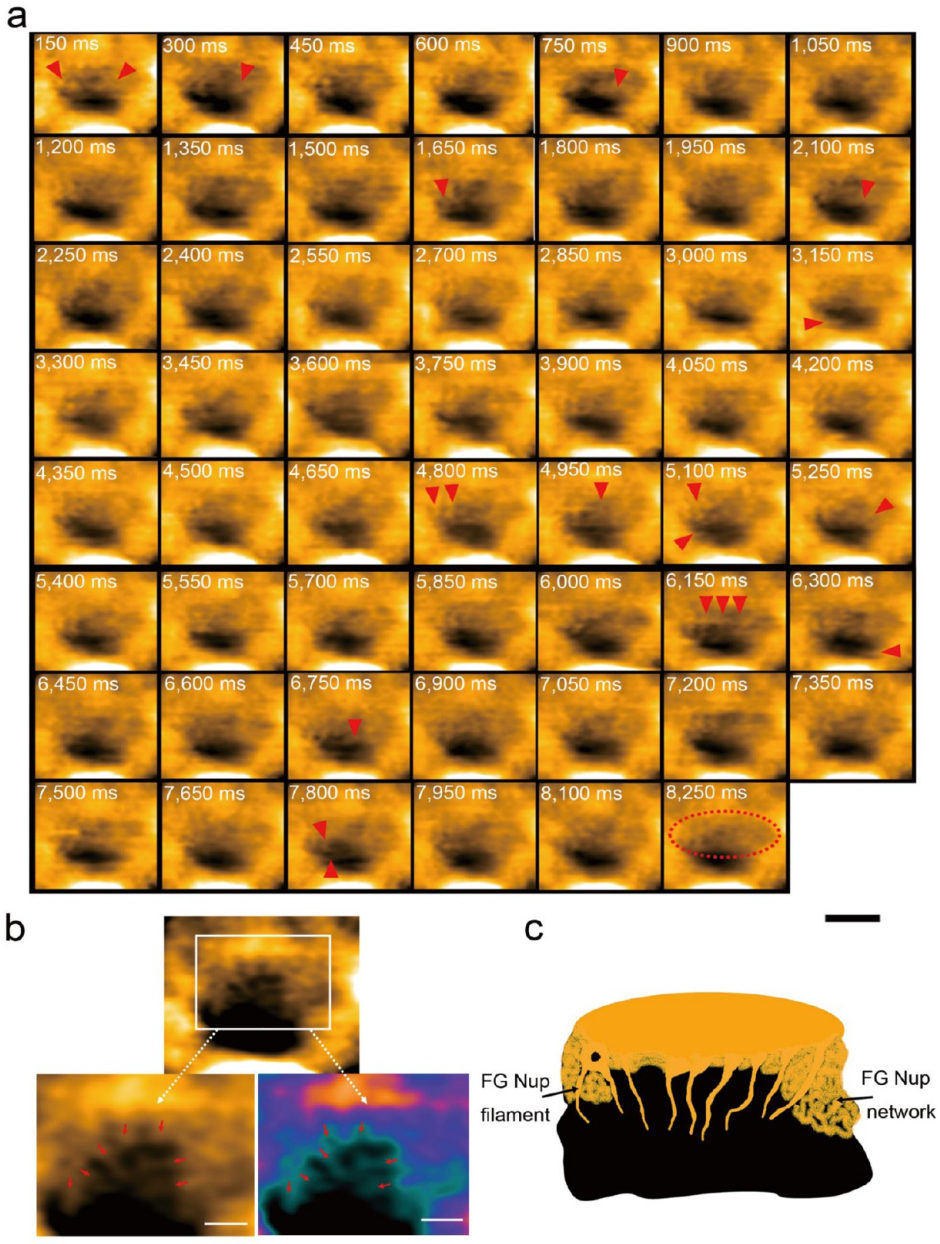

Figure 4. HS-AFM visualization of FG-Nups. (a) Successive HS-AFM images captured at 6.7 frames/s of a 40 × 40 nm^2 area inside the central channel of wild-type (WT) NPCs of HCT116 cells with 200 × 200 pixels. The original HS-AFM frames were processed using an FFT bandpass filter to show only FG filaments entangled inside the central channel (with a maximum of 20 pixels for large structures, a minimum of 3 pixels for small structures, and a tolerance of 5%). Red arrows indicate FG-Nup threads interacting inside the channel and in many frames forming a network, like the one that appeared at time point 8250 ms; scale bar, 10 nm. (b) One frame magnified to show extended FG-Nup threads tethered from the NPC inner ring. (c) Diagram illustrating the FG-Nup threads in (b) showing their extension inside the central channel.

characteristics of virtual gating.[9] The average length of FG-Nups ranged from 5.1 nm (during contraction) to 20.9 nm (during extension) in the control, but we found that after MLN8237 treatment the sequential changes of FG-Nups were found infrequently (ranging from 5 to 11 nm) even under the elapsed time of 300 ms/frame (Figure 5b; Movies 7−10).

To further determine FG-Nup dynamic activities, we concentrated on a 40 × 40 nm^2 scan area squarely on the entrance to the aqueous central turnstile enclosed by cytoplasmic filaments. Subsequent playbacks revealed a remarkable reduction in spatiotemporal behavior and a tractability loss of the FG-Nups within the central turnstile (Figure 6a,b; Movies 9, 10). The FG-Nup thickness as measured by cross-sectional height analyses against a spatial analysis was 0.6 ± 0.3 nm (in control pores; n = 20) compared with 0.2 ± 0.2 nm (in MLN8237-treated pores; n = 20) (Figure 6c,d). In MLN8237-treated pores, the FG-Nup thickness over time was dramatically reduced (Figure 6e). Furthermore, the FG-Nup tether points and flexibility appeared to be lost in these pores (Movies 7−10). Thus, the results of cross-sectional analyses inside the central channel indicate that the spatiotemporal behavior of the bristle FG-Nups and FG-Nups density is radically reduced after MLN8237 treatment (Figure 6c−f; Supplemental Figure 6b; Movies 7−10).

DOI: 10.1021/acsnano.7b00906
ACS Nano 2017, 11, 5567−5578

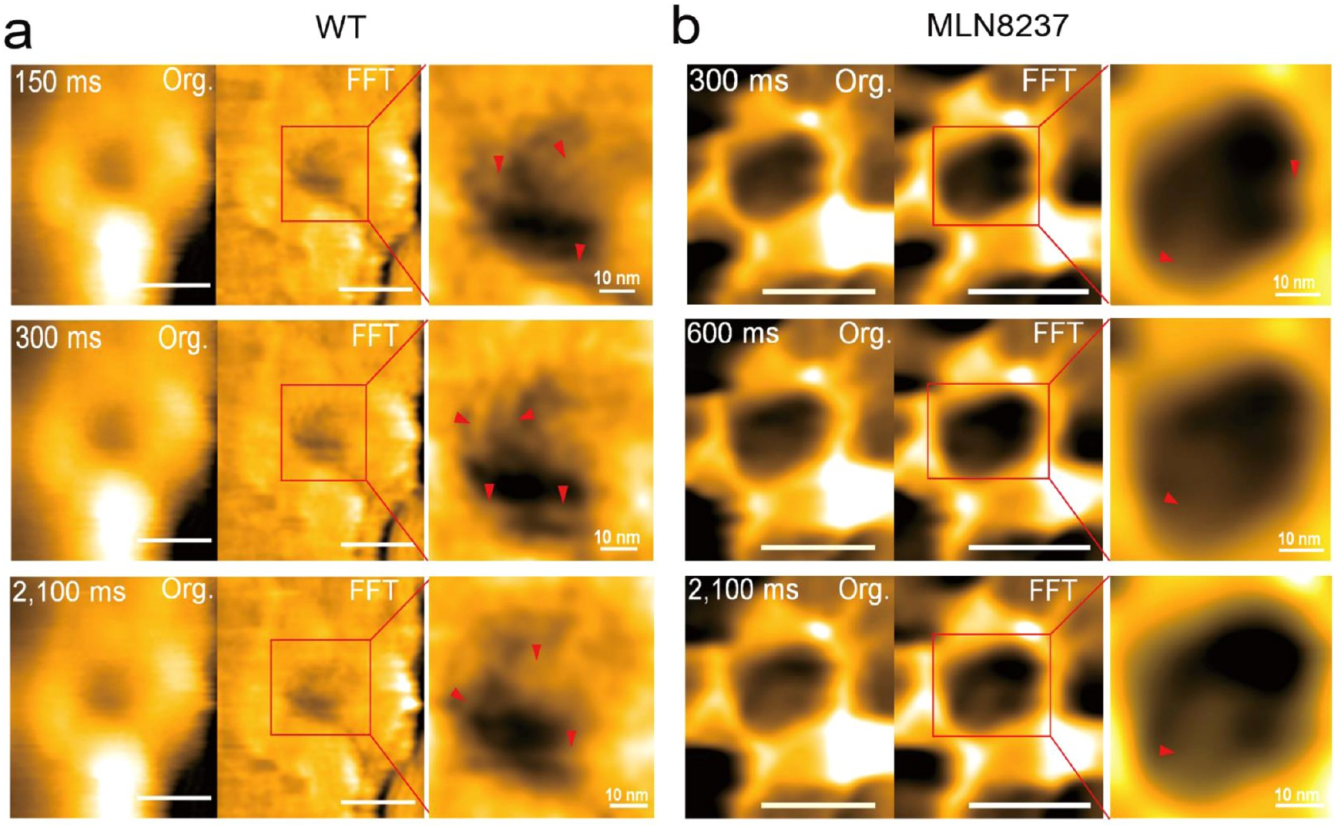

Figure 5. FG-Nups barrier analysis by HS-AFM. (a) Original and FFT-processed frames are shown in this graph to demonstrate the presence of FG-Nups inside the central channel. Red arrows indicate rapid changes in FG-Nups in three different frames of WT NPC (speed = 6.7 frames/s). (b) Original and FFT-processed frames of MLN8237-treated NPC are shown to demonstrate the loss of FG-Nups inside the central channel after cell death induction. Red arrows indicate the remaining FG-Nups, observed in only a few frames (speed = 3.3 frames/s).

In the past decade, HS-AFM has been established and used for the visualization of biomolecules in dynamic action at a high spatiotemporal resolution without disturbing their function;[22] however, visualization of live intracellular organelles, such as the nucleus or mitochondria, is still very challenging due to cantilever tip sizes and morphologies, native sample buffering and immobilization strategies, measurement conditions, and other nanoscale mechanical parameters. Here, unlike with other conventional snapshot or static measurements of "average-out" imaging techniques, we directly visualized native and drug-treated FG-Nups by HS-AFM. Our HS-AFM observations show that FG-Nups have a wriggle brush-like appearance, and we further speculate a "spiders/spidermen working inside the sticky cobweb" model for the process of central channel shuttling or gene gating by the nuclear pore[44] (Figure 7; Movies 9, 10).

Despite the many efforts of various groups to determine the native structure and dynamics of disordered FG-Nups and their dynamic conformations and interactions inside the NPC, defining the precise mechanism of nucleocytoplasmic transport has remained elusive.[45−47] Several nuclear translocation models, such as hydrogel/selective phase, virtual gating/polymer brush, forest, or reduction of dimensionality, have been proposed based on previous experimental approaches. However, these models are not totally separate from each other (Supplementary Figure 8). The NPC selective barrier is believed to be an integral overall network,[45] and tracing NPCs in their native working environment should enable a better understanding both of FG-Nup behavior and of how they form the selective barrier. Here, we propose an alternative cobweb-like model dealing with some of the factors neglected by other models, and our study differs from previous work in several ways. First, we investigated the behavior of native NPCs from human colon cancer cells, which have a selective central barrier. Second, we considered that the flexible wriggle motions of FG-Nups inside the NPC channel are likely to be affected by their tethering sites and interactions with the other scaffolding Nups located at the periphery. Third, our data demonstrate that the FG-Nup filaments can change their thickness over time (Figure 6e and Supplementary Figure 4a), which suggests a mechanism different from those proposed in the previous models (Supplementary Figure 8). Fourth, our HS-AFM live recordings highlighted the contributions by the behavior of FG-Nup filaments within an existing central plug, for which most biophysical and dynamic details have yet to be verified (Supplemental Figure 4; Movie 11).

Further studies are necessary to investigate the differing behaviors of these native FG pliable filaments in an empty NPC as compared with those in a plugged NPC. Moreover, although the MLN8237 treatment data shown in Figure 5b and Figure 6e provide some insight into the native behavior of these filaments under stress conditions, additional studies on this topic are needed. Our tentative cobweb model does not completely exclude the other models (Figure 7 and Supplementary Figure 8); the features of the tangled cobweb network recall the characteristics of the virtual gating[9] and polymer brush[10,14] models. Nevertheless, we also visualized FG-Nup filaments squirming during their interaction with the

DOI: 10.1021/acsnano.7b00906
ACS Nano 2017, 11, 5567−5578

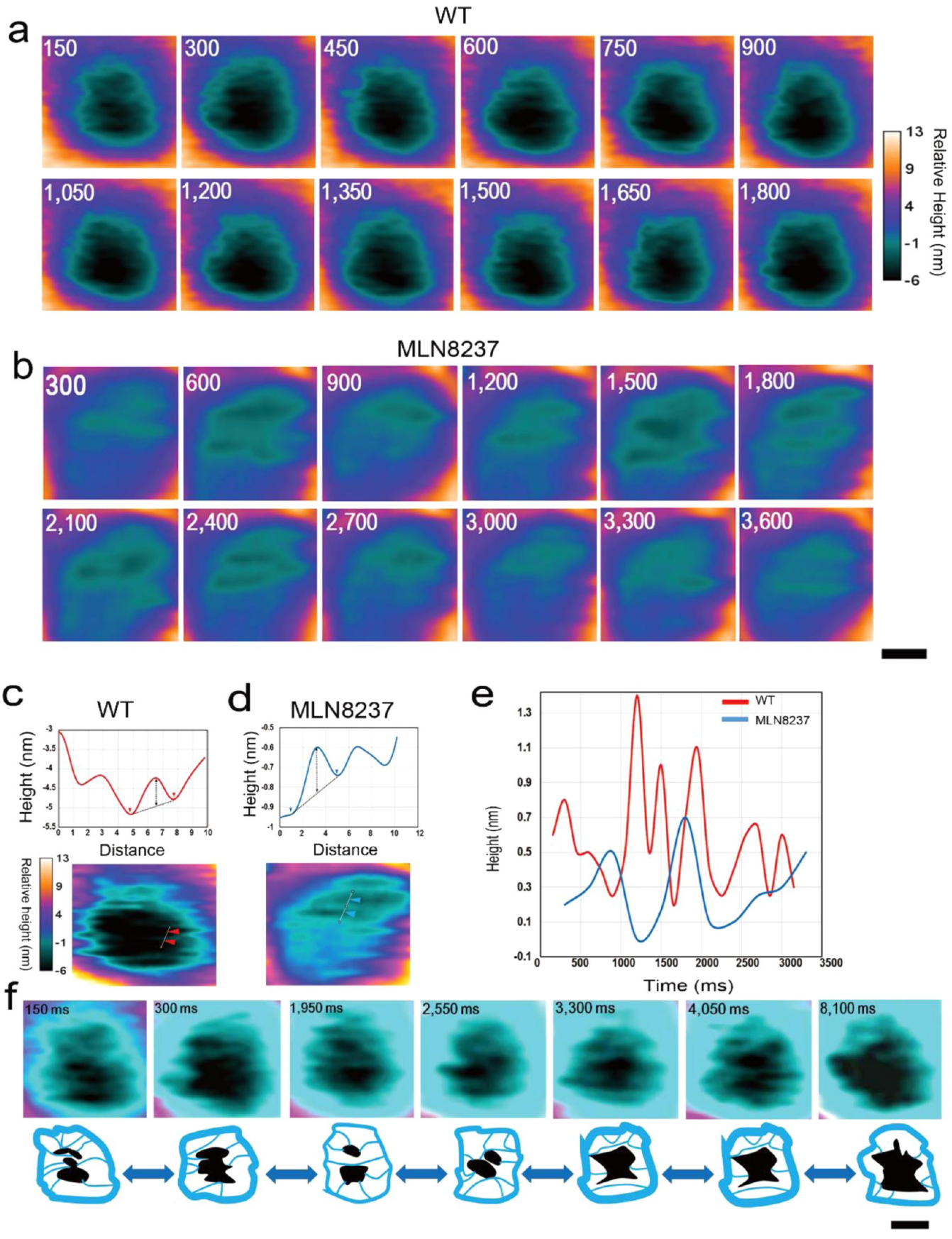

Figure 6. HS-AFM observation of FG-Nups changes after MLN8237 (alisertib) treatment in HCT116 cells. (a) Conformational changes inside the central channel including the FG-Nups barrier of WT pore showing flexible changes of FG-Nups networks inside the channel over the elapsed time with rapid arrangements in the entangled FG-Nups threads (Z-scale = 19 nm, speed = 6.7 frames/s) with 200 × 200 pixels. (b)

DOI: 10.1021/acsnano.7b00906
ACS Nano 2017, 11, 5567−5578

Figure 6. continued

MLN8237-treated pore showing a loss of the FG-Nups network in different successive frames (Z-scale = 19 nm, speed = 3.3 frames/s) with 200 × 200 pixels; scale bar, 10 nm. The numbers on each frame refer to the elapsed time in milliseconds. (c) Cross-sectional analysis inside the central channel showing the average height profile of FG-Nup threads in the WT NPC (n = 20). Average height (thickness) = 0.6 ± 0.3 nm. (d) Cross-sectional analysis inside the central channel showing the average height profile of FG-Nup threads in the MLN8237-treated NPC (n = 20). Average height (thickness) = 0.2 ± 0.2 nm. (e) Heights of FG-Nups measured at different time points plotted against the elapsed time to show the dynamic changes of individual threads in a time-dependent manner in WT and MLN8237-treated NPCs. (f) HS-AFM images showing an extension of the FG-Nups analysis in (a). A 40 × 40 nm^2 area (Z-scale = 19 nm) of the central channel was imaged using the higher speed of 6.7 frames/s to show the behavior of the FG-Nups network. Different frames show conformational changes of FG threads retracting and diffusing and sometimes forming a network that looks like a cobweb.

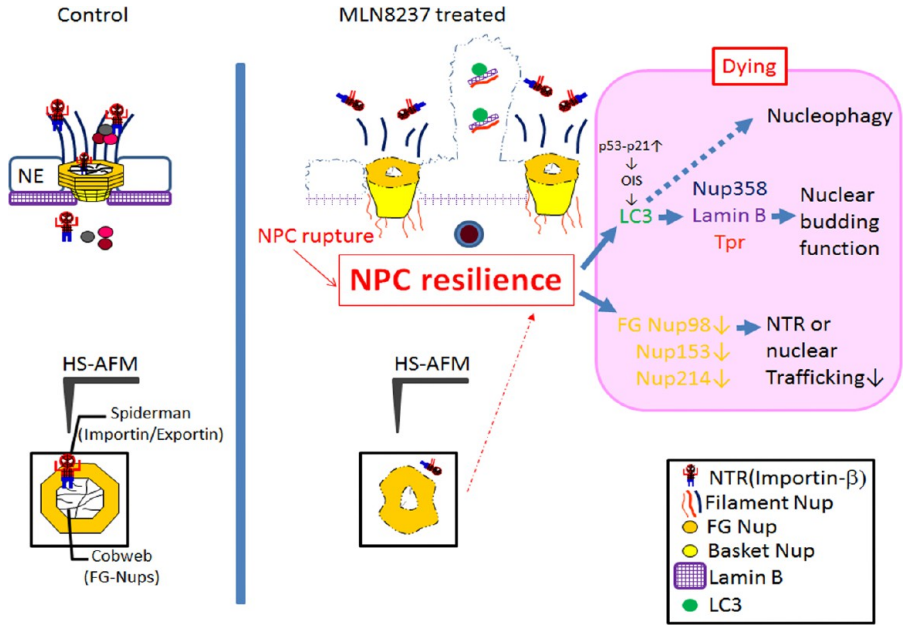

Figure 7. Schematic illustration of the model that the loss of NPC resilience is an irreversible dying code. Structurally, both the "brush model" and "hydrogel model" have been proposed for nuclear transport. We provide an alternative "spiderman-cobweb model" based on our HS-AFM observations (in millisecond scale). Nuclear transport factors (importins/exportins) act as "spidermen", and the cobwebs are mainly composed of FG-Nups. The ultrafast nuclear translocation of cargo occurs by repelling inert material (>5 nm) or melts through the cobweb with waves of salt and pepper (Ran GTP gradient waves). Nuclear transport is assumed to occur in a nanosecond scale; owing to current technical limitations, ultrafast or super-resolution-AFM and other sensitive nanoassays need to be developed before we can validate our "spider-cobweb" hypothesis. Mechanistically, we showed NPC rupture and FG-Nup reduction, which enhanced the LC3 nuclear influx, facilitating the formation of LC3-Lamin B1-Nups subcomplexes and consequently boosting reversible nuclear budding. Unlike other conventional snapshot or static measurements of "average-out" imaging techniques, based on our direct observation *via* high-resolution live cell imaging and HS-AFM videos, we propose that the nanoscopic loss of NPC resilience is an irreversible dying code in cancer cells.

central plug, as shown in Supplementary Figure 4 and Movie 11, and this characteristic is not incorporated into previous models. Whether or not our proposed model will stand the test of time remains to be seen, but it offers an alternative possibility that requires future validation. Compared with the microsecond scale on which molecular fluctuation occurs,[48] our cobweb model speculation was formulated under "slow motion", and confirmation of this model awaits the development of super-resolution ultraspeed AFM.[23]

Importantly, tumor cells are usually distinguished by the occurrence of a lobulated "polymorphic" NE with a range of irregular nuclear grooves and chromatin conformations.[49] There are growing evidences that a wide range of cellular activities highly relevant to tumorigenesis are dependent on the composition and organization of the NE and NPC.[1,50] Thus, how the morphology of NE/NPCs change in normal/healthy cells when they become tumor cells may directly contribute to tumorigenesis. Future comparisons of normal/healthy colon cells, colon cancer cells, and certain anticancer agent-treated cancer cells by HS-AFM analyses will contribute not only to understanding their basic biomedical characteristics but also to developing efficient diagnostics and therapeutics for colorectal cancer.

CONCLUSIONS

Together, our HS-AFM movies strongly support the hypothesis that the molecular kaleidoscopic resilience of individual FG-Nups is lost in the dying nuclei of CRC cells, which facilitates nuclear blebbing and deformation. In conclusion, by mainly using HS-AFM movies and other integrated imaging methods with an inhibitor of Aurora A in human CRC cells, we determined and visualized that a loss of the nanoscopic NPC FG-Nups barrier is another hallmark of the dying code in cancer cells (Figure 7). In this work, we clearly demonstrated that HS-AFM allows the measurement of highly dynamic and disordered intracellular systems. HS-AFM may act as a novel intracellular nanoendoscopy that can be used to visualize other native organelles in cancer cells.

DOI: 10.1021/acsnano.7b00906
ACS Nano 2017, 11, 5567–5578

METHODS

Mechanical Probe Preparations. Small custom-made cantilevers (BL-AC7DS-KU2, Olympus) with a spring constant k of approximately 0.2 N/m and a resonance frequency f = 1.2 MHz in water were used as mechanical probes. The cantilever length, width, and thickness were 6−7 μm, 2 μm, and 90 nm, respectively. A long, amorphous, sharpened carbon tip was grown on the top of each cantilever by EBD using a field emission scanning electron microscope (ELS-7500, Elionix). Cantilever cleaning was achieved by UV/O_3 followed by piranha solution (also known as piranha etch, which is a mixture of sulfuric acid and hydrogen peroxide). EBD was optimized by using a 30 kV accelerating voltage and an irradiation time of 2 min. The use of sharpened and long (~2 μm) carbon tips can improve HS-AFM imaging.

HS-AFM and Fluorescence Microscopy Integration. A high-speed atomic force microscope was equipped with a wide-range HS-AFM scanner and was operated in tapping mode (2 nm free amplitude, ~900 kHz) at room temperature as previously reported.[28] We used the prepared cantilevers in HS-AFM for imaging. The cantilever deflection was identified by detecting the position of the laser beam (670 nm) reflected by the cantilever with a position-sensing two-segmented photodiode. The laser beam was focused onto a cantilever tip using a 20× objective lens (CFI S Plan Fluor ELWD, Nikon). To integrate the HS-AFM with fluorescence microscopy, dichroic filters (MDF-GFP, Thorlabs), an excitation lamp (M470LM, Thorlab), and a CCD camera (DS-Fi2, Nikon) were installed under the HS-AFM system. A solution containing the GFP-labeled NEs was applied on the poly-L-lysine-coated glass stage and used for fluorescence imaging as well as being subjected to nanometer imaging with HS-AFM. The free oscillation amplitude was ~2 nm, and the set-point amplitude was 80−90% of the free amplitude (for details, see the supplementary methods).

Image Processing. The HS-AFM image sequences were processed using ImageJ software (imagej.nih.gov/ij/). A fit polynomial filter was applied with one order in both x and y directions followed by a 2-pixel median filter along the y-axis to reduce the noise. Cross-sectional profiles were acquired to determine the characteristic sizes and heights (for details, see the supplementary methods).

FG-Nups Analysis. Ultraspeed was used to observe the FG-Nups network inside the NPC central turnstile to demonstrate the behavior of this selective barrier in human cells. A speed of 150 ms/frame was used to scan a 40 × 40 nm^2 area inside the central channel. The image resolution could vary subject to the stability, tip quality, and sample roughness. Hence, the FG Nup data shown here were representative of our best resolved data. A fast Fourier transform (FFT) bandpass filter was applied with a maximum of 20 pixels for large structures, a minimum of 3 pixels for small structures, and a tolerance of 5%. FFT processing was used only to filter large and small structures to see the tiny FG-Nups. Later processing of the original data was used to observe the FG-Nups over different time points using image lookup tables. FG threads were observed clearly in Figure 3e−f, Figure 4, and Supplementary Figure 8 (for details, see supplementary methods).

Cell Culture, Transfections, RNA Interference, and Drug Treatments. Human colon cancer HCT116 and SW480 cells were obtained from the American Type Culture Collection (ATCC) and were grown in Dulbecco's modified Eagle's medium (DMEM) supplemented with 10% (v/v) fetal bovine serum (Life Technologies) and 50 U/mL penicillin−streptomycin (Nacalai Tesque). HCT116 and SW480 cells were established from the primary tumors of patients with adenocarcinoma in the right-side (ascending) and the left-side (sigmoid) colon, respectively, and had been characterized to represent the genotypes of microsatellite instability and chromosomal instability pathways, respectively.[51,52] These cell lines are among those most frequently used in biomedical studies for colorectal cancer. SW480 cells were only for live cell imaging in this study. Standard cell culture and transfection procedures were performed as previously described.[53,54]

Antibodies, Immunocytochemistry, and Confocal Microscopy. Anti-mAb414 (MMS-120R) antibody was from COVANCE. Anti-Tpr rabbit polyclonal antibody for confocal microscopy was a kind gift from Dr. Larry Gerace (The Scripps Research Institute). Anti-Tpr (sc-101294) (for immunoblotting) and anti-Tpr (sc-67116) antibodies (for immunoprecipitation) were from Santa Cruz Biotechnology. Anti-GFP antibody (A-6455) was from Life Technologies. Anti-α-tubulin (DM1A) antibody was from Sigma-Aldrich. Antibodies to LC3, p53, and p21 were from Cell Signaling Technology. Secondary antibodies (Alexa Fluor or rhodamine) were from Molecular Probes (Life Technologies).

Confocal, Total Internal Reflection Microscopy and Real-Time Live Cell Imaging. For confocal microscopy, HCT116 or SW480 cells were used as described previously[54,55] and were examined on a confocal microscope (FluoView FV10i, Olympus, objective 60×/1.2). Similarly, for real-time live cell imaging, HCT116 or SW480 GFP-Nups stable cells were visualized by confocal microscopy (FluoView FV10i, Olympus, objective 60×/1.2) or a Nikon Ti-E total internal reflection (TIRF) inverted microscope. The Ti-E was equipped with a perfect focus motorized nosepiece, an additional emission filter wheel, and a CFI APO 100× oil TIRF objective (NA = 1.49). This microscope was capable of detecting single-molecule fluorescence from the manufacturer.

Immunoprecipitation. The CRC cell (HCT116 or SW480) immunoprecipitation assay was performed as previously described.[53,56]

Cell Cycle Profile Analysis. HCT116 or SW480 cells transfected with siRNA were trypsinized, washed twice with phosphate-buffered saline (PBS), and fixed in 70% ethanol at −20 °C overnight. The fixed cells were then resuspended in PBS containing 50 μg/mL RNase A (Nacalai Tesque) and 50 μg/mL propidium iodide (Sigma-Aldrich). Cellular DNA content was analyzed *via* a FACSCanto II (BD Biosciences) with FACS Diva software (BD Biosciences).[53]

Quantitative (q)PCR. RNA was extracted with TRIzol reagent (Invitrogen), and cDNA was synthesized using the ThermoScript RT-PCR System (Invitrogen). Real-time qPCR analysis was performed with the Thermal Cycler Dice real-time system with the SYBR Premix Ex Taq (Takara).[40] The sequence of primers used in this study is listed in Supplemental Table 1. Expression levels of genes analyzed by qPCR were normalized relative to levels of glyceraldehyde-3-phosphate dehydrogenase.

Electron Microscopy. Transmission electron microscopy of HCT116 cells (with or without MLN8237 treatments) was done as described previously, and micrographs were recorded with a JEOL JEM-1200EX at 70−100 kV.[40,55]

Statistical Analysis. Statistical analyses were done in Excel. Data are stated as mean ± SD. Comparisons between groups were resolved using the unpaired t test. $P < 0.05$ was considered statistically significant.

ASSOCIATED CONTENT

Supporting Information

The Supporting Information is available free of charge on the ACS Publications website at DOI: 10.1021/acsnano.7b00906.

Additional figures and tables (PDF)
Movie 1 (AVI)
Movie 2 (AVI)
Movie 3 (AVI)
Movie 4 (AVI)
Movie 5 (AVI)
Movie 6 (AVI)
Movie 7 (AVI)
Movie 8 (AVI)
Movie 9 (AVI)
Movie 10 (AVI)
Movie 11 (AVI)

AUTHOR INFORMATION

Corresponding Author

*Tel (R. Wong): +81-76-264-6250. Fax: +81-76-264-6253. E-mail: rwong@staff.kanazawa-u.ac.jp.

DOI: 10.1021/acsnano.7b00906
ACS Nano 2017, 11, 5567−5578

ORCID

Richard W. Wong: 0000-0002-2131-6595

Author Contributions

T.A. and R.W. designed the NPC-HS-AFM project. M.M.S. performed the HS-AFM experiments and data analysis and prepared the figures. A.K. and R.W. performed biochemical studies, EM, and live cell imaging. U.T. participated in the early stage of this study. A.T. performed TIRM. M.M.S., K.Y., and W.-N.T. performed cantilever preparation, ImageJ graphics, and HS-AFM movies preparation. K.N. developed the fluorescent HS-AFM apparatus for this study. H.M., M.T., and F.Y. gave critical advice and performed data analysis. R.W. supervised the study and wrote the manuscript. All authors have given approval to the final version of the manuscript.

Notes

The authors declare no competing financial interest.

ACKNOWLEDGMENTS

This work was supported by a MEXT/JSPS KAKENHI Grant Number 24227005 (to A.T.); 24117007 (to Y.F.); 15H04928 (to T.M.); and 17H05874, 17K08655 (to R.W.) from MEXT Japan, and by grants from the Extramural Collaborative Research Grant of Cancer Research Institute, Kanazawa University, the Uehara Memorial Foundation, the Suzuken Memorial Foundation, the Asahi Glass Foundation, the Kowa Life Science Foundation, the Sumitomo Foundation, the Mochida Memorial Foundation, the Sagawa Foundation, the Ichiro Kanehara Foundation, and the Takeda Science Foundation (to R.W.). We are grateful to Jan Lammerding for Lamin plasmids. We are especially indebted to Roderick Lim and Bart Hoogenboom for insightful discussions at the 4th Kanazawa Bio-AFM workshop.

REFERENCES

(1) Funasaka, T.; Wong, R. W. The Role of Nuclear Pore Complex in Tumor Microenvironment and Metastasis. *Cancer Metastasis Rev.* **2011**, *30*, 239−251.

(2) Panagiotakopoulou, M.; Bergert, M.; Taubenberger, A.; Guck, J.; Poulikakos, D.; Ferrari, A. A Nanoprinted Model of Interstitial Cancer Migration Reveals a Link Between Cell Deformability and Proliferation. *ACS Nano* **2016**, *10*, 6437−6448.

(3) Yuan, Y.; Chen, S.; Paunesku, T.; Gleber, S. C.; Liu, W. C.; Doty, C. B.; Mak, R.; Deng, J.; Jin, Q.; Lai, B.; Brister, K.; Flachenecker, C.; Jacobsen, C.; Vogt, S.; Woloschak, G. E. Epidermal Growth Factor Receptor Targeted Nuclear Delivery and High-Resolution Whole Cell X-Ray Imaging of Fe_3O_4@TiO_2 Nanoparticles in Cancer Cells. *ACS Nano* **2013**, *7*, 10502−10517.

(4) Wong, R. W. Nuclear Pore Complex: From Structural View to Chemical Tools. *Chem. Biol.* **2015**, *22*, 1285−1287.

(5) Denais, C. M.; Gilbert, R. M.; Isermann, P.; McGregor, A. L.; te Lindert, M.; Weigelin, B.; Davidson, P. M.; Friedl, P.; Wolf, K.; Lammerding, J. Nuclear Envelope Rupture and Repair During Cancer Cell Migration. *Science* **2016**, *352*, 353−358.

(6) Wong, R. W.; D'Angelo, M. Linking Nucleoporins, Mitosis, and Colon Cancer. *Cell Chem. Biol.* **2016**, *23*, 537−539.

(7) Obado, S. O.; Brillantes, M.; Uryu, K.; Zhang, W.; Ketaren, N. E.; Chait, B. T.; Field, M. C.; Rout, M. P. Interactome Mapping Reveals the Evolutionary History of the Nuclear Pore Complex. *PLoS Biol.* **2016**, *14*, e1002365.

(8) Huo, S.; Jin, S.; Ma, X.; Xue, X.; Yang, K.; Kumar, A.; Wang, P. C.; Zhang, J.; Hu, Z.; Liang, X. J. Ultrasmall Gold Nanoparticles As Carriers for Nucleus-Based Gene Therapy Due to Size-Dependent Nuclear Entry. *ACS Nano* **2014**, *8*, 5852−5862.

(9) Rout, M. P.; Aitchison, J. D.; Magnasco, M. O.; Chait, B. T. Virtual Gating and Nuclear Transport: The Hole Picture. *Trends Cell Biol.* **2003**, *13*, 622−628.

(10) Lim, R. Y.; Huang, N. P.; Koser, J.; Deng, J.; Lau, K. H.; Schwarz-Herion, K.; Fahrenkrog, B.; Aebi, U. Flexible Phenylalanine-Glycine Nucleoporins as Entropic Barriers to Nucleocytoplasmic Transport. *Proc. Natl. Acad. Sci. U. S. A.* **2006**, *103*, 9512−9517.

(11) Hulsmann, B. B.; Labokha, A. A.; Gorlich, D. The Permeability of Reconstituted Nuclear Pores Provides Direct Evidence for the Selective Phase Model. *Cell* **2012**, *150*, 738−751.

(12) Vovk, A.; Gu, C.; Opferman, M. G.; Kapinos, L. E.; Lim, R. Y.; Coalson, R. D.; Jasnow, D.; Zilman, A. Simple Biophysics Underpins Collective Conformations of the Intrinsically Disordered Proteins of the Nuclear Pore Complex. *eLife* **2016**, *5*, e10785.

(13) Yamada, J.; Phillips, J. L.; Patel, S.; Goldfien, G.; Calestagne-Morelli, A.; Huang, H.; Reza, R.; Acheson, J.; Krishnan, V. V.; Newsam, S.; Gopinathan, A.; Lau, E. Y.; Colvin, M. E.; Uversky, V. N.; Rexach, M. F. A Bimodal Distribution of Two Distinct Categories of Intrinsically Disordered Structures with Separate Functions in FG Nucleoporins. *Mol. Cell. Proteomics* **2010**, *9*, 2205−2224.

(14) Lim, R. Y.; Deng, J. Interaction Forces and Reversible Collapse of a Polymer Brush-Gated Nanopore. *ACS Nano* **2009**, *3*, 2911−2918.

(15) Dange, T.; Grunwald, D.; Grunwald, A.; Peters, R.; Kubitscheck, U. Autonomy and Robustness of Translocation Through the Nuclear Pore Complex: A Single-Molecule Study. *J. Cell Biol.* **2008**, *183*, 77−86.

(16) Cardarelli, F.; Lanzano, L.; Gratton, E. Capturing Directed Molecular Motion in the Nuclear Pore Complex of Live Cells. *Proc. Natl. Acad. Sci. U. S. A.* **2012**, *109*, 9863−9868.

(17) Bestembayeva, A.; Kramer, A.; Labokha, A. A.; Osmanovic, D.; Liashkovich, I.; Orlova, E. V.; Ford, I. J.; Charras, G.; Fassati, A.; Hoogenboom, B. W. Nanoscale Stiffness Topography Reveals Structure and Mechanics of the Transport Barrier in Intact Nuclear Pore Complexes. *Nat. Nanotechnol.* **2015**, *10*, 60−64.

(18) Andersen, H.; Parhamifar, L.; Hunter, A. C.; Shahin, V.; Moghimi, S. M. AFM Visualization of Sub-50nm Polyplex Disposition to the Nuclear Pore Complex without Compromising the Integrity of the Nuclear Envelope. *J. Controlled Release* **2016**, *244*, 24−29.

(19) Kramer, A.; Liashkovich, I.; Oberleithner, H.; Ludwig, S.; Mazur, I.; Shahin, V. Apoptosis Leads to a Degradation of Vital Components of Active Nuclear Transport and a Dissociation of the Nuclear Lamina. *Proc. Natl. Acad. Sci. U. S. A.* **2008**, *105*, 11236−11241.

(20) Shahin, V. Cellular Transport: Gatekeepers of the Nucleus. *Nat. Nanotechnol.* **2016**, *11*, 658−659.

(21) Preiner, J.; Horner, A.; Karner, A.; Ollinger, N.; Siligan, C.; Pohl, P.; Hinterdorfer, P. High-Speed AFM Images of Thermal Motion Provide Stiffness Map of Interfacial Membrane Protein Moieties. *Nano Lett.* **2015**, *15*, 759−763.

(22) Ando, T. High-Speed AFM Imaging. *Curr. Opin. Struct. Biol.* **2014**, *28*, 63−68.

(23) Ando, T.; Uchihashi, T.; Scheuring, S. Filming Biomolecular Processes by High-Speed Atomic Force Microscopy. *Chem. Rev.* **2014**, *114*, 3120−3188.

(24) Uchihashi, T.; Kodera, N.; Ando, T. Guide to Video Recording of Structure Dynamics and Dynamic Processes of Proteins by High-Speed Atomic Force Microscopy. *Nat. Protoc.* **2012**, *7*, 1193−1206.

(25) Sakiyama, Y.; Mazur, A.; Kapinos, L. E.; Lim, R. Y. Spatiotemporal Dynamics of the Nuclear Pore Complex Transport Barrier Resolved by High-Speed Atomic Force Microscopy. *Nat. Nanotechnol.* **2016**, *11*, 719−723.

(26) Colom, A.; Casuso, I.; Rico, F.; Scheuring, S. A Hybrid High-Speed Atomic Force-Optical Microscope for Visualizing Single Membrane Proteins on Eukaryotic Cells. *Nat. Commun.* **2013**, *4*, 2155.

(27) Ando, T.; Kodera, N.; Takai, E.; Maruyama, D.; Saito, K.; Toda, A. A High-Speed Atomic Force Microscope for Studying Biological Macromolecules. *Proc. Natl. Acad. Sci. U. S. A.* **2001**, *98*, 12468−12472.

(28) Shibata, M.; Uchihashi, T.; Ando, T.; Yasuda, R. Long-Tip High-Speed Atomic Force Microscopy for Nanometer-Scale Imaging in Live Cells. *Sci. Rep.* **2015**, *5*, 8724.

DOI: 10.1021/acsnano.7b00906
ACS Nano 2017, 11, 5567−5578

(29) Diguilio, A. L.; Glavy, J. S. Depletion of Nucleoporins from Hela Nuclear Pore Complexes to Facilitate the Production of Ghost Pores for *In Vitro* Reconstitution. *Cytotechnology* **2013**, *65*, 469−479.
(30) Beck, M.; Forster, F.; Ecke, M.; Plitzko, J. M.; Melchior, F.; Gerisch, G.; Baumeister, W.; Medalia, O. Nuclear Pore Complex Structure and Dynamics Revealed by Cryoelectron Tomography. *Science* **2004**, *306*, 1387−1390.
(31) Beck, M.; Hurt, E. The Nuclear Pore Complex: Understanding its Function Through Structural Insight. *Nat. Rev. Mol. Cell Biol.* **2017**, *18*, 73−89.
(32) Taylor, J. P. A PR Plug for the Nuclear Pore in Amyotrophic Lateral Sclerosis. *Proc. Natl. Acad. Sci. U. S. A.* **2017**, *114*, 1445−1447.
(33) Shi, K. Y.; Mori, E.; Nizami, Z. F.; Lin, Y.; Kato, M.; Xiang, S.; Wu, L. C.; Ding, M.; Yu, Y.; Gall, J. G.; McKnight, S. L. Toxic Prn Poly-Dipeptides Encoded by the C9orf72 Repeat Expansion Block Nuclear Import and Export. *Proc. Natl. Acad. Sci. U. S. A.* **2017**, *114*, E1111−E1117.
(34) Asally, M.; Yasuda, Y.; Oka, M.; Otsuka, S.; Yoshimura, S. H.; Takeyasu, K.; Yoneda, Y. Nup358, a Nucleoporin, Functions As a Key Determinant of the Nuclear Pore Complex Structure Remodeling During Skeletal Myogenesis. *FEBS J.* **2011**, *278*, 610−621.
(35) Perez-Terzic, C.; Behfar, A.; Mery, A.; van Deursen, J. M.; Terzic, A.; Puceat, M. Structural Adaptation of the Nuclear Pore Complex in Stem Cell-Derived Cardiomyocytes. *Circ. Res.* **2003**, *92*, 444−452.
(36) Faustino, R. S.; Behfar, A.; Groenendyk, J.; Wyles, S. P.; Niederlander, N.; Reyes, S.; Puceat, M.; Michalak, M.; Terzic, A.; Perez-Terzic, C. Calreticulin Secures Calcium-Dependent Nuclear Pore Competency Required for Cardiogenesis. *J. Mol. Cell. Cardiol.* **2016**, *92*, 63−74.
(37) Pitts, T. M.; Bradshaw-Pierce, E. L.; Bagby, S. M.; Hyatt, S. L.; Selby, H. M.; Spreafico, A.; Tentler, J. J.; McPhillips, K.; Klauck, P. J.; Capasso, A.; Diamond, J. R.; Davis, S. L.; Tan, A. C.; Arcaroli, J. J.; Purkey, A.; Messersmith, W. A.; Ecsedy, J. A.; Eckhardt, S. G. Antitumor Activity of the Aurora A Selective Kinase Inhibitor, Alisertib, Against Preclinical Models of Colorectal Cancer. *Oncotarget* **2016**, *7*, 50290−50301.
(38) Melichar, B.; Adenis, A.; Lockhart, A. C.; Bennouna, J.; Dees, E. C.; Kayaleh, O.; Obermannova, R.; DeMichele, A.; Zatloukal, P.; Zhang, B.; Ullmann, C. D.; Schusterbauer, C. Safety and Activity of Alisertib, an Investigational Aurora Kinase A Inhibitor, in Patients with Breast Cancer, Small-Cell Lung Cancer, Non-Small-Cell Lung Cancer, Head and Neck Squamous-Cell Carcinoma, and Gastro-Oesophageal Adenocarcinoma: A Five-Arm Phase 2 Study. *Lancet Oncol.* **2015**, *16*, 395−405.
(39) Manfredi, M. G.; Ecsedy, J. A.; Chakravarty, A.; Silverman, L.; Zhang, M.; Hoar, K. M.; Stroud, S. G.; Chen, W.; Shinde, V.; Huck, J. J.; Wysong, D. R.; Janowick, D. A.; Hyer, M. L.; Leroy, P. J.; Gershman, R. E.; Silva, M. D.; Germanos, M. S.; Bolen, J. B.; Claiborne, C. F.; Sells, T. B. Characterization of Alisertib (MLN8237), an Investigational Small-Molecule Inhibitor of Aurora A Kinase Using Novel *In Vivo* Pharmacodynamic Assays. *Clin. Cancer Res.* **2011**, *17*, 7614−7624.
(40) Funasaka, T.; Tsuka, E.; Wong, R. W. Regulation of Autophagy by Nucleoporin Tpr. *Sci. Rep.* **2012**, *2*, 878.
(41) Larsson, L. G. Oncogene- and Tumor Suppressor Gene-Mediated Suppression of Cellular Senescence. *Semin. Cancer Biol.* **2011**, *21*, 367−376.
(42) Dou, Z.; Xu, C.; Donahue, G.; Shimi, T.; Pan, J. A.; Zhu, J.; Ivanov, A.; Capell, B. C.; Drake, A. M.; Shah, P. P.; Catanzaro, J. M.; Ricketts, M. D.; Lamark, T.; Adam, S. A.; Marmorstein, R.; Zong, W. X.; Johansen, T.; Goldman, R. D.; Adams, P. D.; Berger, S. L. Autophagy Mediates Degradation of Nuclear Lamina. *Nature* **2015**, *527*, 105−109.
(43) Miyagi, A.; Tsunaka, Y.; Uchihashi, T.; Mayanagi, K.; Hirose, S.; Morikawa, K.; Ando, T. Visualization of Intrinsically Disordered Regions of Proteins by High-Speed Atomic Force Microscopy. *ChemPhysChem* **2008**, *9*, 1859−1866.
(44) Blobel, G. Gene Gating: A Hypothesis. *Proc. Natl. Acad. Sci. U. S. A.* **1985**, *82*, 8527−8529.
(45) Yang, W. 'Natively Unfolded' Nucleoporins in Nucleocytoplasmic Transport: Clustered or Evenly Distributed? *Nucleus* **2011**, *2*, 10−16.
(46) Weis, K. The Nuclear Pore Complex: Oily Spaghetti or Gummy Bear? *Cell* **2007**, *130*, 405−407.
(47) Schmidt, H. B.; Gorlich, D. Transport Selectivity of Nuclear Pores, Phase Separation, and Membraneless Organelles. *Trends Biochem. Sci.* **2016**, *41*, 46−61.
(48) Chattopadhyay, K.; Elson, E. L.; Frieden, C. The Kinetics of Conformational Fluctuations in an Unfolded Protein Measured by Fluorescence Methods. *Proc. Natl. Acad. Sci. U. S. A.* **2005**, *102*, 2385−2389.
(49) Chow, K. H.; Factor, R. E.; Ullman, K. S. The Nuclear Envelope Environment and its Cancer Connections. *Nat. Rev. Cancer* **2012**, *12*, 196−209.
(50) Simon, D. N.; Rout, M. P. Cancer and the Nuclear Pore Complex. *Adv. Exp. Med. Biol.* **2014**, *773*, 285−307.
(51) Gayet, J.; Zhou, X. P.; Duval, A.; Rolland, S.; Hoang, J. M.; Cottu, P.; Hamelin, R. Extensive Characterization of Genetic Alterations in a Series of Human Colorectal Cancer Cell Lines. *Oncogene* **2001**, *20*, 5025−5032.
(52) Ahmed, D.; Eide, P. W.; Eilertsen, I. A.; Danielsen, S. A.; Eknaes, M.; Hektoen, M.; Lind, G. E.; Lothe, R. A. Epigenetic and Genetic Features of 24 Colon Cancer Cell Lines. *Oncogenesis* **2013**, *2*, e71.
(53) Kobayashi, A.; Hashizume, C.; Dowaki, T.; Wong, R. W. Therapeutic Potential of Mitotic Interaction Between the Nucleoporin Tpr and Aurora Kinase A. *Cell Cycle* **2015**, *14*, 1447−1458.
(54) Hashizume, C.; Kobayashi, A.; Wong, R. W. Down-Modulation of Nucleoporin Ranbp2/Nup358 Impaired Chromosomal Alignment and Induced Mitotic Catastrophe. *Cell Death Dis.* **2013**, *4*, e854.
(55) Hashizume, C.; Moyori, A.; Kobayashi, A.; Yamakoshi, N.; Endo, A.; Wong, R. W. Nucleoporin Nup62 Maintains Centrosome Homeostasis. *Cell Cycle* **2013**, *12*, 3804−3816.
(56) Nakano, H.; Funasaka, T.; Hashizume, C.; Wong, R. W. Nucleoporin Translocated Promoter Region (Tpr) Associates with Dynein Complex, Preventing Chromosome Lagging Formation During Mitosis. *J. Biol. Chem.* **2010**, *285*, 10841−10849.

DOI: 10.1021/acsnano.7b00906
ACS Nano 2017, 11, 5567−5578